Enhancing Interfacial Li^+ Transport and Dielectric Properties in Poly(ethylene oxide)-Based All-Solid Electrolytes via Inactive g-C_3N_4 Nanosheets Filler Incorporation

Zhixuan Li [a,b,c,1], Weijian Zhang [a,b,c,1], Yue Chen [a,b,*], Qiaoquan Lin[a,b], Long Zhang [a,b,*], Jianming Tao [a,b], Oleg V. Kolosov [d], Jiaxin Li [a,b], Yingbin Lin [a,b], Zhigao Huang [a,c,*]

[a] College of Physics and Energy, Fujian Normal University, Fujian Provincial Key Laboratory of Quantum Manipulation and New Energy Materials, Fuzhou 350117, China

[b] Fujian Provincial Engineering Technical Research Centre of Solar-Energy Conversion and Stored Energy, Fuzhou 350117, China

[c] Fujian Provincial Collaborative Innovation Centre for Advanced High-Field Superconducting Materials and Engineering, Fuzhou 350117, China

[d] Physics Department, Lancaster University, Lancaster LA1 4YB, UK

The Faraday Institution, Quad One, Becquerel Avenue, Harwell Campus, Didcot, OX11 0RA, UK

Corresponding author: yuechen@fjnu.duc.cn; longzhang2013@163.com; zghuang@fjnu.edu.cn;

[1]Zhixuan Li and Weijian Zhang contribute equally

Abstract

The advancement of all-solid-state Li metal batteries (ASSLMBs) faces a major challenge in the growth of lithium dendrites on the anode-electrolyte interface. In this study, we propose a dual-filler approach using poly(ethylene oxide) (PEO)-based solid polymer electrolytes (SPEs) that combine $Li_{1.4}Al_{0.4}Ti_{1.6}(PO_4)_3$ (LATP) ion-conductive particles with graphitic carbon nitride (g-C_3N_4) nanosheets. Analysis through second harmonic resonance enhanced electrostatic force microscopy reveals that the g-C_3N_4 additives form nano-capacitors at the SPE-lithium interface, effectively reducing sudden changes in current densities. The distribution of relaxation time constant (DRT) measurements confirms that the g-C_3N_4 filler suppresses uncontrolled Li dendrite growth, effectively mitigating battery aging caused by anode interfacial degradation. Furthermore, X-ray photoelectron spectroscopy (XPS) analysis indicates that the nitrogen-containing organic groups in g-C_3N_4 are reduced to form a stable interfacial layer with lithium metal. As a result of these enhancements, the electrolyte demonstrates remarkable interfacial stability in Li/Li symmetrical cells at 0.65 mA/cm^2 and delivers promising performance in assembled Li-$LiFePO_4$ batteries, achieving a reversible capacity of 121.6 mAh/g at 1 C after 200 cycles. These findings highlight the potential of dual-filler PEO-based SPEs for promoting interfacial lithium-ion transport in all-solid-state Li metal batteries.

Introduction

The energy density limitations of commercial liquid Li-ion batteries (LIBs) based on graphite anodes results in the increasingly urgent demands for high-energy-density batteries [1]. All-solid-state Li metal batteries (ASSLMBs) using solid electrolytes (SEs) have been widely studied as the most promising alternative due to their high energy density [2, 3]. Typical SEs such as oxides (e.g., LLZO [4], LLTO [5]) and sulfides (e.g., Li_6PS_5Cl [6], $Li_{10}GeP_2S_{12}$ [7]) have been extensively investigated due to their high ionic conductivity, high Li-ion transference number and suitable mechanical strength [8]. However, the large interfacial impedance caused by solid-solid point contact between electrolyte and electrode, as well as the non-negligible electronic conductivity, unavoidably leads to dendrites penetrating SEs and causing dangerous short circuits [9]. Currently, solid polymer electrolytes (SPEs), such as poly(ethylene oxide) (PEO) [10], poly(vinylidene fluoride) (PVDF) [11] and polyacrylonitrile (PAN) [12], are expected to be excellent solid electrolytes due to their good mechanical flexibility, low cost, and easy processability [13].

Although the flexibility of SPEs can reduce the interfacial impedance, the detrimental side reactions [14] and Li dendrite growth still hinder their applications [15]. Creating composites of inorganic fillers in polymer matrix in SPEs is shown to be an efficient strategy to improve the interfacial electrochemical compatibility and suppress the growth of Li dendrites [16-20]. However, the role of inorganic fillers in suppressing the formation of Li dendrites remains elusive. In recent years, several theories have been proposed to explain the formation of Li dendrites [21]. The widely accepted space-charge layer theory [22], proposed by Chazalviel, suggests that the space-charge layer caused by the excessive depletion of anions near Li metal anodes is the cause of the uneven Li deposition. In other words, a uniform Li plating can be achieved by the smooth Li^+ flux [23-25] and the highly ionic-conductive solid-electrolyte interphase (SEI) [26, 27] on the SPEs/Li interface. The majority of studies

suggested that the ideal filler should be able to regulate Li^+ flux near the SEs/Li interface and increase the Li^+ transfer number by anchoring anions [28-35].

Recently, graphitic carbon nitride (g-C_3N_4) with a two-dimensional layered structure and large specific surface area has been used as an inactive filler in SPEs [36, 37]. Hu et al. verified the strong interaction between g-C_3N_4 and the anions in Li salts, which induced a high Li^+ transference number [38]. However, it is worth noting that with g-C_3N_4 acting as an inactive filler, it's excess inactive in SPEs would drastically reduce the ionic conductivity. It is therefore reasonable to expect that the overall electrochemical performance of SEPs can be optimized by mixing active filler (Lithium conductor) with g-C_3N_4, which can fully take advantage of the percolation effect of highly ionic-conductive active fillers, and the anchoring effect of inactive filler on salt anions. Furthermore, the inactive filler particles in PEO matric can be treated as distributed multiple localized nano-capacitances embedded in SPEs, making dielectric properties of inactive filler playing an important role in the ion diffusion and electrolyte polarization in SPEs. While g-C_3N_4 is more widely used as an interface "stabilizer" [39-42], the effects of higher electrical permittivity (compared with PEO) on regulating interface Li^+ flux have not yet been well-explored [43].

Herein, to understand the underlying optimization mechanism of g-C_3N_4 for ASSLMBs in SPEs, we used a dual-filler PEO-based SPE loaded with ion-conductive particles of $Li_{1.4}Al_{0.4}Ti_{1.6}(PO_4)_3$(LATP) and 2D structured g-C_3N_4. It is found that the optimized contents of active filler (LATP) in SPEs serve as the percolation network for lithium diffusion, while the strong interaction between inactive filler (g-C_3N_4) and TFSI anion leads to improvement of Li^+ transference number. The dielectric properties of the optimized SPE were enhanced by g-C_3N_4, leading to a minimized anion depletion region on the surface of the anode. Moreover, the nitrogen-containing organic groups in g-C_3N_4 adsorb to the Li metal anode regulating Li^+ flux. The above effects synergistically suppress the uncontrolled growth of Li dendrites and

effectively delay the battery aging caused by anode interface degradation.

Experimental section

Synthesis of g-C_3N_4 powder: g-C_3N_4 powders were prepared by thermal condensation using melamine as a precursor, heating at 550 ℃ in an air atmosphere for 4 hours with a heating rate of 10 ℃/min. 10 g of melamine (Sigma, >99%) was placed in a quartz boat at the center of the tube furnace. The slits at both sides of the tube furnace were kept open to maintain the ambient pressure. After natural cooling, the prepared product was collected in an agate mortar, and ground for further use.

Synthesis of electrolyte film: All types of electrolytes with different fillers were prepared by the solution casting method. Poly(ethylene oxide) (PEO, Mv=300000, Macklin) and LiTFSI (Duoduo chemical) were first dissolved in acetonitrile at a ratio of [PEO]: Li^+=16:1. Then, commercial ionic conductor $Li_{1.4}Al_{0.4}Ti_{1.6}(PO_4)_3$ (LATP, ~600 nm, Kejing) was added in different weight ratios. After mechanical stirring, it was vacuum-dried for 24 hours, cut into 16 mm discs and stored in a glove box for further use. In this paper, the electrolytes containing 0 *w*t.%, 5 *w*t.%, 10 *w*t.%, 15 *w*t.% and 20 *w*t.% LATP are designated as PEO-LiTFSI (PL), 5%LATP, 10%LATP, 15%LATP (PLL) and 20%LATP. The electrolyte composed with 10 *w*t.% LATP and 5 *w*t.% g-C_3N_4 was designated as PLLG.

Materials characterization: X-ray diffraction patterns of all electrolyte films and powders were characterized by Rigaku MiniFlex II using Cu Kα line (λ=1.5405 Å). Morphological characterization of all samples was determined using a field-emission scanning electron microscope (FESEM; HITACHI, SU-8010). The elemental valence states of g-C_3N_4 and Li metal surfaces were characterized by X-ray Photoelectron Spectroscopy (ESCALAB 250Xi; Thermo Scientific). The Thermogravimetric (TG) and Differential scanning calorimetry (DSC) curves of all electrolytes were tested on a Netzsch STA449F3 analyzer from 25 °C to 600 °C

with a temperature ramp of 10 °C per minute under a nitrogen flow. The mechanical properties of the electrolyte film were tested by auto tensile tester (C610H; Labthink).

Electrochemical and dielectric property measurements: The ionic conductivity of the electrolyte at different temperatures was obtained by electrochemical impedance spectroscopy (EIS) with a frequency range from 4 MHz to 1 Hz at the temperature from 30 to 70 °C, the electrolyte was sandwiched between two stainless steel sheets (SS) to assemble a coin cell (SS/SS cell) and tested using a Zahner Zennium IM6 electrochemical workstation with an AC amplitude of 10 mV, with ionic conductivity calculated by Equation 1.

$$\sigma = \frac{L}{R_b S} \quad \text{(Eq 1)}$$

Where R_b is the bulk impedance in the EIS, and L and S are the thickness and area of the stainless steel electrodes, respectively. Assembled SS/Li cells were characterized using linear sweep voltammetry (LSV) from 3 to 6 V at a scan rate of 1 mV/s at 60 °C on a CHI 1000C electrochemical workstation. The Li-ion transference number (τ_{Li^+}) was tested by assembling a Li/Li symmetrical cell and testing the DC polarization curve and interface impedance on the Zahner Zennium IM6 electrochemical workstation. Li-ion transference number (τ_{Li^+}) was calculated by Equation 2.

$$\tau_{Li^+} = \frac{I_{ss}(\Delta V - I_0 R_0)}{I_0(\Delta V - I_{ss} R_{ss})} \quad \text{(Eq 2)}$$

where I_{ss} and I_0 are the initial and steady currents, and R_{ss} and R_0 are the interface impedance before and after the polarization test, respectively. ΔV is the DC polarization voltage of 20 mV. The all-solid-state battery was assembled in an argon atmosphere glove box, and the $LiFePO_4$ cathode was coated on aluminum foil with a ratio of $LiFePO_4$: carbon black: PVDF=7: 2: 1. The battery performance was measured in LAND 2001A battery testing system in the voltage range of 2.6-3.8 V at 60 ℃. The Li plating and stripping curves were tested on the LAND 2001A battery testing system at 60 ℃ with two current densities of 0.25 mA/cm^2

and 0.65 mA/cm^2, respectively.

The effective dielectric constant of SPEs was measured by impedance spectroscopy and dielectric force microscopy (DFM) at the 2nd harmonic of electrical excitation tuned to the free fundamental resonance of the cantilever, providing resonance enhancement of DFM signal [44]. Dielectric properties of the SPEs are illustrated based on the plots of the real (ε') which can be calculated from:

$$\varepsilon' = -\frac{dZ''}{\omega A \varepsilon_0 (Z'^2 + Z''^2)} \quad \text{(Eq 3)}$$

where ω is the angular frequency, ε_0 is the vacuum permittivity, A is the area of the blocking electrode, d is the thickness of the SPE, and Z'' is the imaginary and Z' the real parts of impedance, respectively [45-46]. The cantilever used in DFM is Pt coated conductive force modulation tip with a force constant of about 0.3 N/m and a free resonance frequency of about 69 kHz. DFM was performed in Dual-pass mode, in which the topography scan uses mechanical tapping amplitude at 1st free resonance frequency (69 kHz) followed by the lift-scan with lift high ~20 nm. During the lift-scan, the mechanical excitation was turned off and the cantilever was excited by the AC sinusoidal voltage (tuned at around 34 kHz corresponding to half of the cantilever free resonance frequency) between the sample and the AFM tip. The oscillation of the cantilever was detected at the 2nd harmonic of electrical excitation frequency (69 kHz) with the signal-to-noise ratio of dielectric response significantly improved. In this measure configuration, the tip apex and sample can be treated as a parallel capacitance. The force acted on the conductive tip can be written as:

$$F = -\frac{\partial\left(\frac{1}{2}CV^2\right)}{\partial Z} = -\frac{1}{2}\frac{\partial C}{\partial Z}(V_{AC} + V_{CPD})^2 \quad \text{(Eq 4)}$$

where C is the capacitance between the tip apex and conductive sample substrate (Lithium metal), Z is the height of the tip lift, $V_{AC} = A_0 \sin\omega t$ is the electrical excitation voltage, where ω is the circular frequency of the electrical excitation, and V_{CPD} is the contact potential

difference between tip and sample. According to Equation 4, the force acting on the cantilever at the frequency of 2ω can be written as:

$$F_{2\omega} = \frac{1}{4}\frac{\partial C}{\partial z}A_0^2 \cos 2\omega t \quad \text{(Eq 5)}$$

where A_0 is the amplitude of AC excitation. Since $\frac{\partial C}{\partial z}$ is proportional to the dielectric constant, the measured tip-sample interaction force at 2ω ($A_{2\omega}$) can be used to qualitatively represent the dielectric constant of the sample surface at each image pixel.

Result and discussion

1. Optimizing the contents of active filler (LATP) to reach the Li^+ percolation threshold

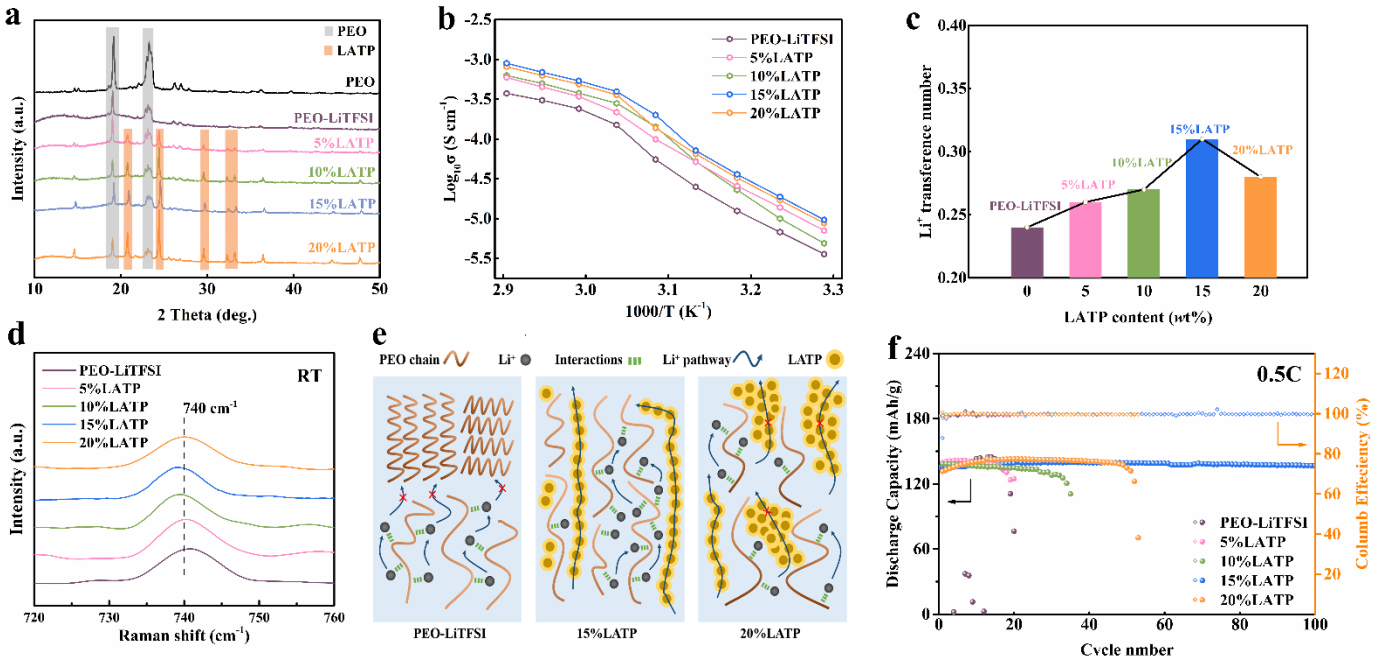

Fig. 1. (a) XRD Θ–2Θ patterns of electrolytes. (b) Arrhenius plots and (c) Li-ion transference number of electrolytes with different LATP contents. (d) Raman spectra of electrolytes with different LATP content in the range of 720 cm^{-1} to 760 cm^{-1}. (e) Schematic illustration of LATP forming a percolation network in PEO matrix. (f) Cycling performance of $LiFePO_4$-Li cells using SPEs with different LATP contents at 0.2 C at 60 °C.

The percolation threshold of active filler content was explored in details in Fig. 1. Fig. 1a

shows the XRD patterns of electrolyte films with different LATP contents, the peak intensity of PEO at around 19° and 23° decreased with the increase of LATP composition, indicating that the addition of LATP reduces the crystallinity of PEO and thus increases the proportion of amorphous region [47]. This reduced crystallinity of PEO with the increased filler contents is also confirmed by DSC (Fig. S1). The Arrhenius plots of electrolytes with various filler contents are shown in Fig. 1b, the electrolyte with a filler content of 15*wt*% has the highest ionic conductivity of 5.39×10^{-4} S cm^{-1}. The decrease in the ionic conductivity of the 20% LATP indicates that the excess filler will reduce the ion transport efficiency. This can be attributed to the agglomeration effect [48] of filler inside the solid electrolyte as confirmed by SEM in the supplementary information (SI) Fig. S2. Li-Li symmetric cells based on various electrolytes were assembled to test the Li-ion transference number (τ_{Li^+}) [49]. Figs. S3 and S4 (SI) present the time-current curves and Electrochemical Impedance Spectroscopy (EIS) spectra, with the results were summarized in Fig. 1c. The increased trend of τ_{Li^+} from 0 *wt.*% to 15 *wt.*% LATP filler indicates that the τ_{Li^+} could be enhanced by optimizing the LATP content, while the decreased τ_{Li^+} in 20% LATP may be due to agglomeration caused by the excess filler (Fig. S2). Raman spectroscopy was used to determine the chemical state of LiTFSI in each electrolyte. The Raman spectra in the range of 720-760 cm^{-1} are shown in Fig. 1d, the peak at 740 cm^{-1} can be attributed to the dissociated $TFSI^-$ anion group in LiTFSI, and the shifting of peak toward the lower wavenumber indicates that the addition of LATP could enhance the dissociation of LiTFSI in the PEO matrix [50]. The LiTFSI was dissociated most efficiently in 15% LATP, indicating the highest ratio of the free lithium ions in 15 *wt.*% LATP. Moreover, by optimizing the filler contents at around 15 *wt.*%, the electrochemical oxidation potential of the PEO-LiTFSI is increased from 4.0 V to 4.5 V (Fig. S5a), and the mechanical Young's modulus is improved from 3.71 MPa to 7.49 MPa (Fig. S5b) due to the reinforcement effect by LATP filler. More importantly, no obvious interfacial degradation in static contact between

15% LATP and Li at room temperature (Fig. S6a). To sum up, as sketched in Fig. 1e, the optimized contents (~15 *wt.*%) of LATP filler results in segmental mobility improvement, abundant percolation networks were formed through the uniform distribution of LATP in the PEO, and both electrochemical stability and mechanical properties were drastically improved. As a result, there were no obvious overpotential fluctuations observed in Li/15% LATP/Li cell (Fig. S6b), indicating the high reversibility of plating and stripping of Li-ions at the Li electrode interface during cycling [51].

Additionally, Li/$LiFePO_4$ all-solid-state batteries were assembled to evaluate the compatibility of electrodes and electrolytes in Fig. 1f. At 0.5 C at 60°C, the $LiFePO_4$/15% LATP/Li cell exhibited the best cycle performance with a capacity of 136.6 mAh/g and a high capacity retention after 100 cycles (The cycle performance test at 0.2 C is shown in Fig. S7). This can be attributed to the improved ionic conductivity and the optimized interfacial stability [52] as confirmed by the EIS measurements in SI Fig. S8. The rate performance and the polarization voltage at the high current density of each SPEs were compared in SI Fig. S9, in which the lowest polarization voltage of 15%LATP was observed. The smaller electrode polarization is also confirmed by the narrowed gap of oxidation and reduction peaks in the cyclic voltammetry (CV) curves in SI Fig. S10.

However, we did notice that, the cycle stability and high-rate performance of $LiFePO_4$/15% LATP/Li cell do not meet our expectations, with capacity dropping significantly when increasing the cycle number over 100^{th} or for the current density higher than 0.5 C. The interfacial stability and ion transportation at higher current density also had to be further improved.

2. Synergetic improvement of bulk ionic conductivity and interfacial dielectric permittivity by g-C_3N_4 additives

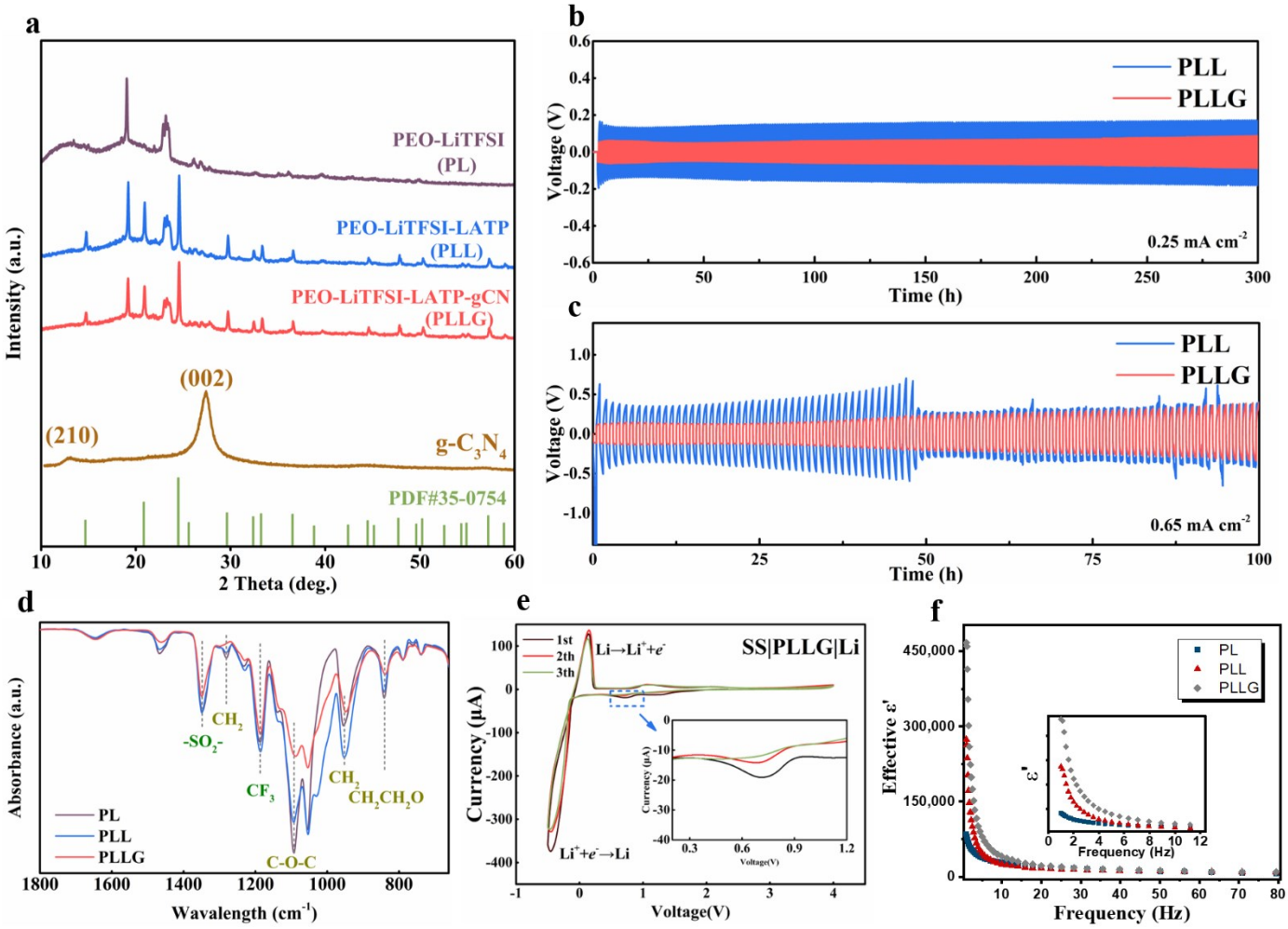

Fig. 2. (a) XRD pattern of PL, PLL, PLLG and g-C_3N_4 powder. Cycling performance of Li/Li symmetrical cells based on PLL and PLLG with a current density of (b) 0.25 mA cm^{-2} and (c) 0.65 mA cm^{-2} at 60 °C. (d) FT-IR spectra of PL, PLL and PLLG. (e) CV profiles of SS/PLlG/Li cell. (f) The effective dielectric constant of PL, PLL and PLLG SPEs.

To further improve the interfacial stability and ion transportation at higher current density, we created a composite of 5 *wt*% g-C_3N_4 and 10 *wt*% LATP in PEO based on the discussion in section 1. As shown in Fig. 2a, there are two characteristic peaks at 13° and 27° in the XRD pattern of g-C_3N_4, which can be attributed to the (210) and (002) planes [53], indicating that the as-prepared g-C_3N_4 has the reported melon structure. The chemical structures are also characterised by FTIR (Fig. S11) and X-ray photoelectron spectroscopy (XPS) (Fig. S12), in

which abundant nitrogen contain groups (C-N, C=N and N-H) were detected, indicating that there are abundant amino groups on the surface of g-C_3N_4 [54, 55].

After the g-CN was added to SPEs, the surface roughness and filler uniformity did not change according to our SEM and TG measurements in SI Figs. S13-15. Compared with the XRD pattern of PLL in Fig. 2a, the intensity of the characteristic peaks (at ~19° and ~23°) in PLLG is lower, indicating that the addition of g-C_3N_4 can further reduce the crystallinity. This is because the strong interaction between g-C_3N_4 and PEO segments that leads to the improvement in ionic conductivity to 6.46×10^{-4} S cm^{-1} (Fig. S16). Importantly, the ionic conductivity of composite electrolytes with different g-C_3N_4 contents was also summarized in Fig. S16, with the increase of ionic conductivity in PLL+2% g-C_3N_4 and the decrease in PLL+8% g-C_3N_4 both indicating that the appropriate inactive filler content could improve Li-ion transport kinetics.

The effect of the g-C_3N_4 additives on suppressing lithium dendrites was confirmed in the Li-ions plating/stripping tests, using the voltage profiles at a current density of 0.25 mA/cm^2 at 60℃ as shown in Fig. 2b. PLLG shows a low overpotential at the initial stage of the cycle, and the overpotential was stable without a short circuit within 300 h, implying a lower interface impedance between the electrolyte and Li metal. Fig. 2c presents the results of the Li-Li symmetrical cells at a high current density of 0.65 mA/cm^2, with the voltage drop observed in the Li/PLL/Li cell at 49 h indicating that the lithium dendrites are connected internally causing a short circuit, while the Li/PLLG/Li cell shows a low overpotential of about 40 mV within 100 h. These results suggested that the g-C_3N_4 additives can significantly improve the stability of the electrolyte against the Li metal anode. However, the LSV tests of each electrolyte (Fig. S17) show that there is no significant difference in the redox potentials of PLL and PLLG. Such improvement in the stability of Li plating/stripping cannot be explained by the enhanced ion conductivity and transfer number (0.41) alone (Fig. S18). We speculate that such

improvement is related to the different chemical environments of lithium-ions and the formation of SEI at the lithium metal anode interface.

The FTIR spectra of each type of electrolyte are shown in Fig. 2d, the peaks at 954 cm^{-1}, 1092 cm^{-1} and 1280 cm^{-1} corresponding to the asymmetric stretching, symmetric stretching and deformation vibration of C-O-C [56], respectively. Compared with other electrolytes, the intensities of all three above-mentioned peaks decreased significantly, indicating that there was a strong interaction between g-C_3N_4 filler and PEO, which is also supported by the observed intensity decrease of the deformation vibration of CH_2CH_2O at the peak of 841 cm^{-1}. The strong interaction between g-C_3N_4 and the ether oxygen groups on the chain segments can reduce the complexation between Li-ions and ether oxygen groups. Moreover, the intensity of the CF_3 asymmetric stretching vibration peak at 1187 cm^{-1} and the -SO_2- asymmetric stretching vibration peak at 1347 cm^{-1} also decreased significantly [32,38,57], indicating that g-C_3N_4 adsorbs the $TFSI^-$ anion group in the Li-salt and inhibits the facial movement of anions during the charge/discharge. Furthermore, PLLG has a better cathodic stability and a more reversible plating and stripping reversibility than PL and PLL (Fig. 2e and Fig. S19), as well as better mechanical properties (Fig. S19).

Dielectric analysis was used to identify the ionic transportation and related dielectric relaxation behavior in PL, PLL and PLLG. It can be seen from Fig. 2f that, at the low frequency, the effective dielectric constant of all electrolytes reaches the maximum value because of the space charge polarization at the interfaces [58], which reflects the capacitive contribution of the polarization of ion species and ionic mobility conductors. One can notice that, at the low-frequency region, the sharpest rise in the effective dielectric constant for the PLLG sample indicates the highest ionic conductivity.

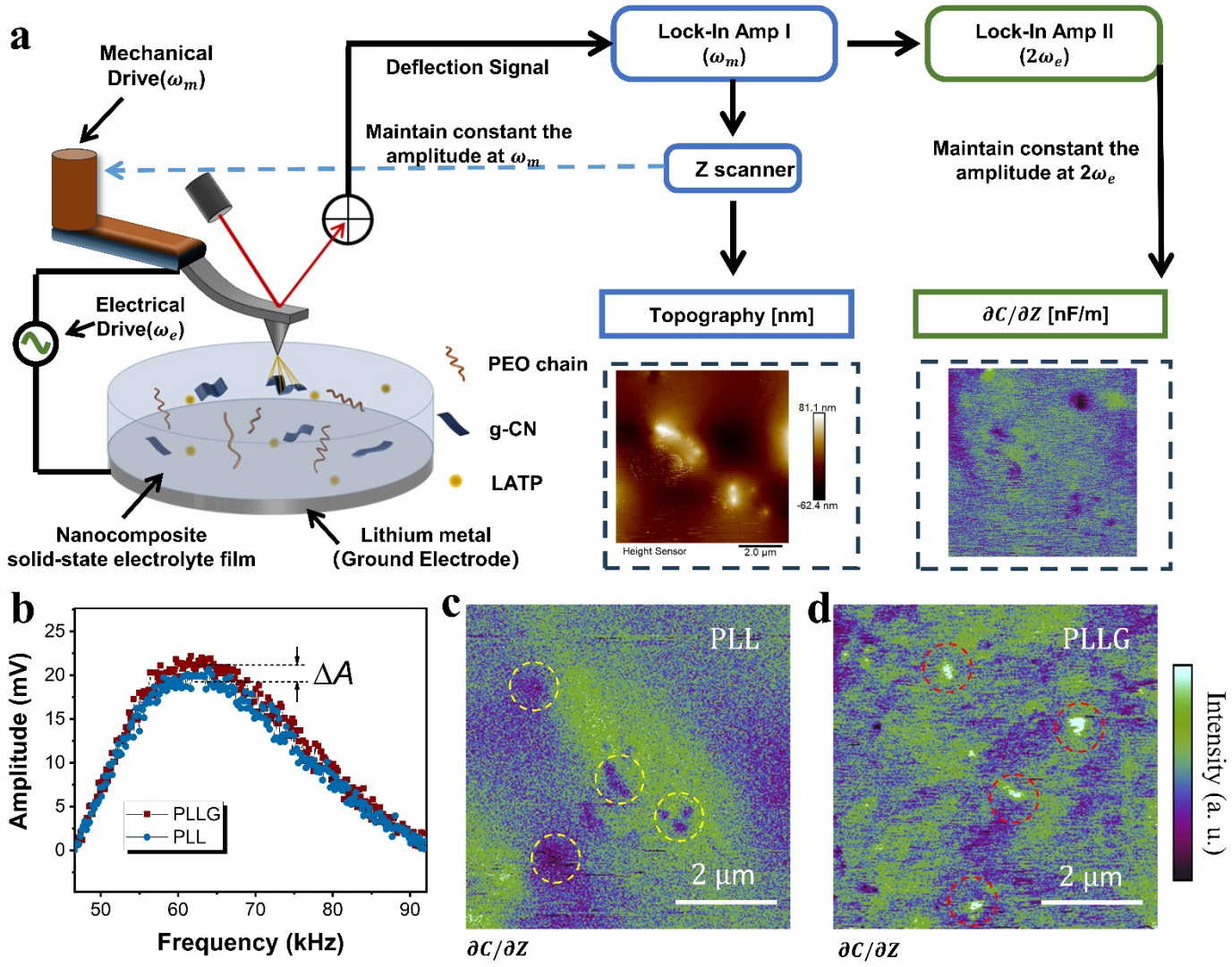

Fig. 3. (a) Schematic of dielectric force microscopy (DFM) derived from dual-pass resonance-enhanced 2nd harmonic electrical force microscopy. Surface morphology and dielectric response images of SPEs can be recorded simultaneously. (b) The average second harmonic oscillation amplitude of cantilever on PLL and PLLG solid electrolyte surface. The dielectric force response map of (c) PLL and (d) PLLG measured by DFM.

It has been reported that an appropriate dielectric constant of SPEs can generate a moderate opposite internal dielectric polarization field inside on SPE-anode interface and inhibit lithium dendrite formation [43, 59]. We introduce dielectric force microscopy (DFM) in the second harmonic enhanced mode (see Experimental Methods) to further study the nanoscale filler-PEO interfacial dielectric permittivity in SPEs. Fig. 3a shows the detailed schematic of DFM. The AC excitation was applied between the conductive tip and the lithium metal with a thin

layer of PLL and PLLLG coated on the surface. The dielectric property underneath the tip at each image pixel was compared by recording the tip oscillation amplitude at the 2nd harmonic of electrical excitation (see Equation 5), which is proportional to the dielectric permittivity of the space between the tip and lithium. As compared in Fig. 3b, about 15% higher amplitude was detected in PLLG compared to PLL, indicating a 15% higher dielectric constant at the excitation frequency. The $\frac{\partial C}{\partial z}$ images on PLLG and PLL surface were further compared as shown in Figs. 3c and 3d. At ~kHz excitation range, the LATP particles will have a lower value (dark contrast) in $\frac{\partial C}{\partial z}$ channel due to the immobilized lithium ions (Fig. S21b). As shown in Fig. 3c, the PLL surface contains an inhomogeneous dielectric permittivity distribution, with the dark region (low dielectric constant region inside the yellow circles) linked to the LATP nano-particles. By contrast, the PLLG surface shows more uniform distribution of dielectric permittivity (Fig. 3d), and the bright spots (inside the red circles) corresponding to the g-C_3N_4 additives clearly observed. These "bright spots", with higher dielectric permittivity, can serve as the nano-capacitors that can act as a "shock absorber" for the lithium plating and striping to inhibit any sudden changes in the lithium flux. Meanwhile, at the electrolyte-anode interface, a higher dielectric region derived from the g-C_3N_4 additive particles can result in a dipole layer arranged near the anode surface that can also guide the lithium ions into a more uniform path [60].

3. Improved overall battery performance and interfacial compatibility

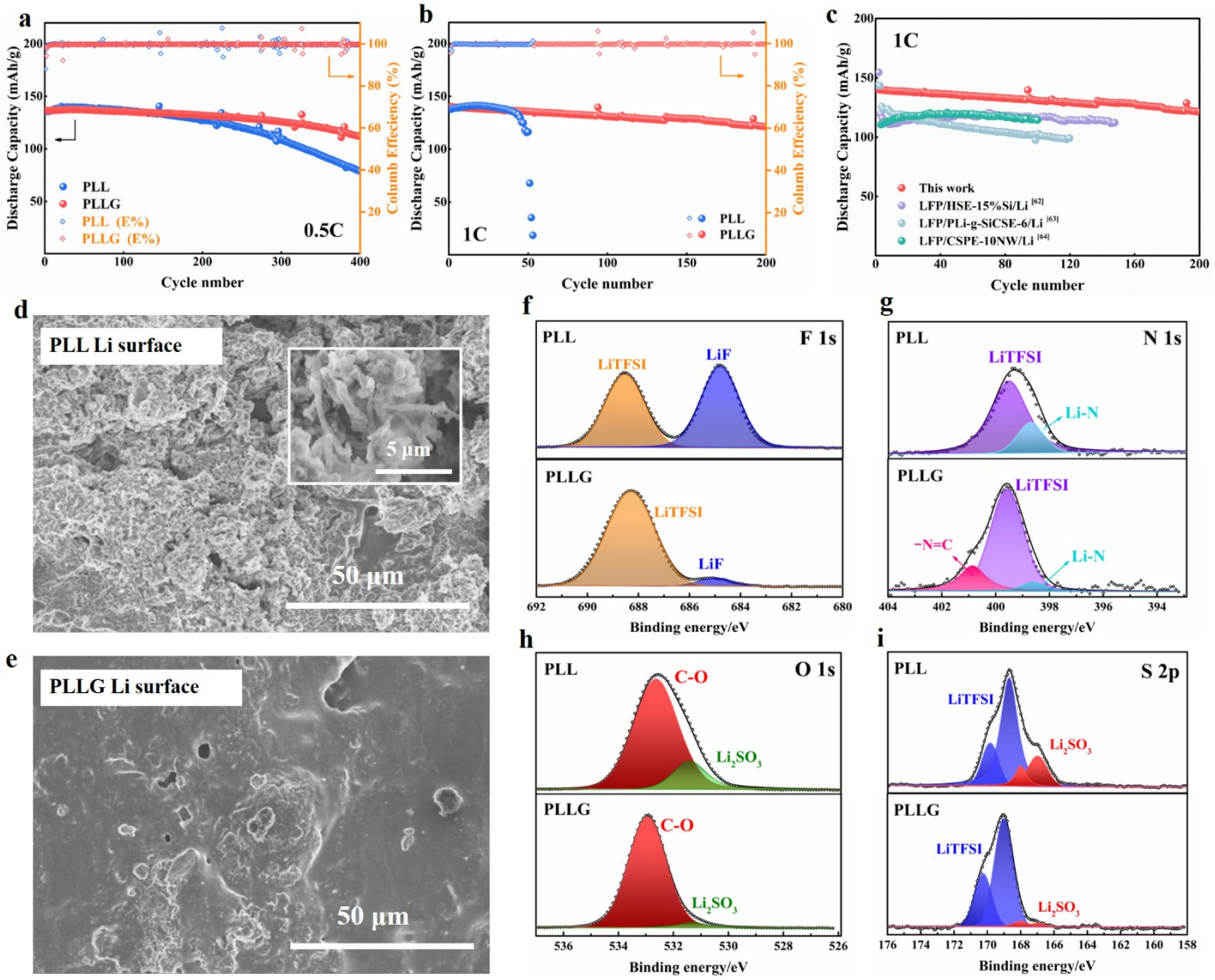

Fig. 4. Cycling performance of $LiFePO_4$/PLL/Li cell and $LiFePO_4$/PLLG/Li cell at (a) 0.2 C and (b) 0.5 C at 60 ℃. (c) The comparation of cycling performance of other recently reported SPEs at 1C at 60 °C. Li anode surface morphology of (d) $LiFePO_4$/PLL/Li cell and (e) $LiFePO_4$/PLLG/Li cell after cycling at 1 C at 60 ℃. XPS spectra of cycled Li surface (f) F *1s* (g) N 1s (h) O 1s (i) S 2p at 1 C.

$LiFePO_4$/Li all-solid-state batteries were assembled to evaluate the performance of the electrolytes. Fig. 4a shows the cycle performance and coulombic efficiency of batteries based on each electrolyte at a current density of 0.5 C at 60℃, the $LiFePO_4$/PLLG/Li battery delivers 112.1 mAh/g reversible specific capacity with 82% capacity retention after 400 cycles and a

low polarization charge-discharge curve (Fig. S21c). In contrast, $LiFePO_4$/PLL/Li only has a specific capacity of 77.3 mAh/g and a retention of 56% after 400 cycles. In Fig. 4b, the specific capacity of $LiFePO_4$/PLL/Li dropped drastically after only 50 cycles, with PLLG delivering a much more stable capacity curve with 121.6 mAh/g reversible capacity and a high capacity retention of 86%. Meanwhile, $LiFePO_4$/PLLG/Li exhibited extremely stable interfacial polarization during cycling at 1 C current density (Fig. S22a). The EIS spectra after cycles at 1 C (Fig. S22b) also indicate an effectively suppressed interfacial impedance increase. The rate performance of each cell is shown in Fig. S23, and $LiFePO_4$/PLLG/Li also present slightly higher capacity compared to the $LiFePO_4$/PLL/Li cell at all charge/discharge rates. It is worth noting that the 1 C cycle performance of our PLLG is better than the recently reported SPEs (Fig. 4c) [61-63], while the capacity attenuation and large overpotential were still found in the batteries with non-optimised contents of g-CN (Fig. S24).

To understand the lithium deposition behavior on the Li metal anode surface, SEM images of the Li metal anode surface cycled in PLL and PLLG at 1 C are captured as shown in Figs. 4d and 4e, respectively. Compared with the flaky lithium dendrites in PLL, PLLG has a flatter lithium metal surface after cycling, indicating that Li-ions can be deposited uniformly at the interface. XPS was employed to further analyze the elemental content and valence on the Li metal anode surface. In the F *1s* spectra are shown in Fig. 4f, a decrease in the proportion of LiF (684.8 eV) peak was observed after adding g-C_3N_4 [64]. In the O *1s* spectra shown in Fig. 4h, the peak at 531.2 eV [65] can be assigned to Li_2SO_3, with the proportion of Li_2SO_3 in PLLG decreased significantly compared with that in PLL, which was also proved in the S *2p* spectra (Fig. 4i). Since both LiF and Li_2SO_3 are formed by the decomposition of $TFSI^-$ anion, the decrease in the proportion of both components at the Li metal anode interface indicates the decomposition of the anion group is suppressed. The weakening of the peak at 398.6 eV assigned to Li_3N in the N 1s spectra (Fig. 4g) [66] also suggests smaller decomposition

reaction of anion groups. The peak at 400.7 eV can be assigned to nitrogen-containing groups (C-N=C) adsorbed on the Li metal anode surface [67], which has been proven to have a strong interaction with Li-ions and promote the uniform distribution of Li-ions at the interface, leading to a Li dendrite-free interface during cycling.

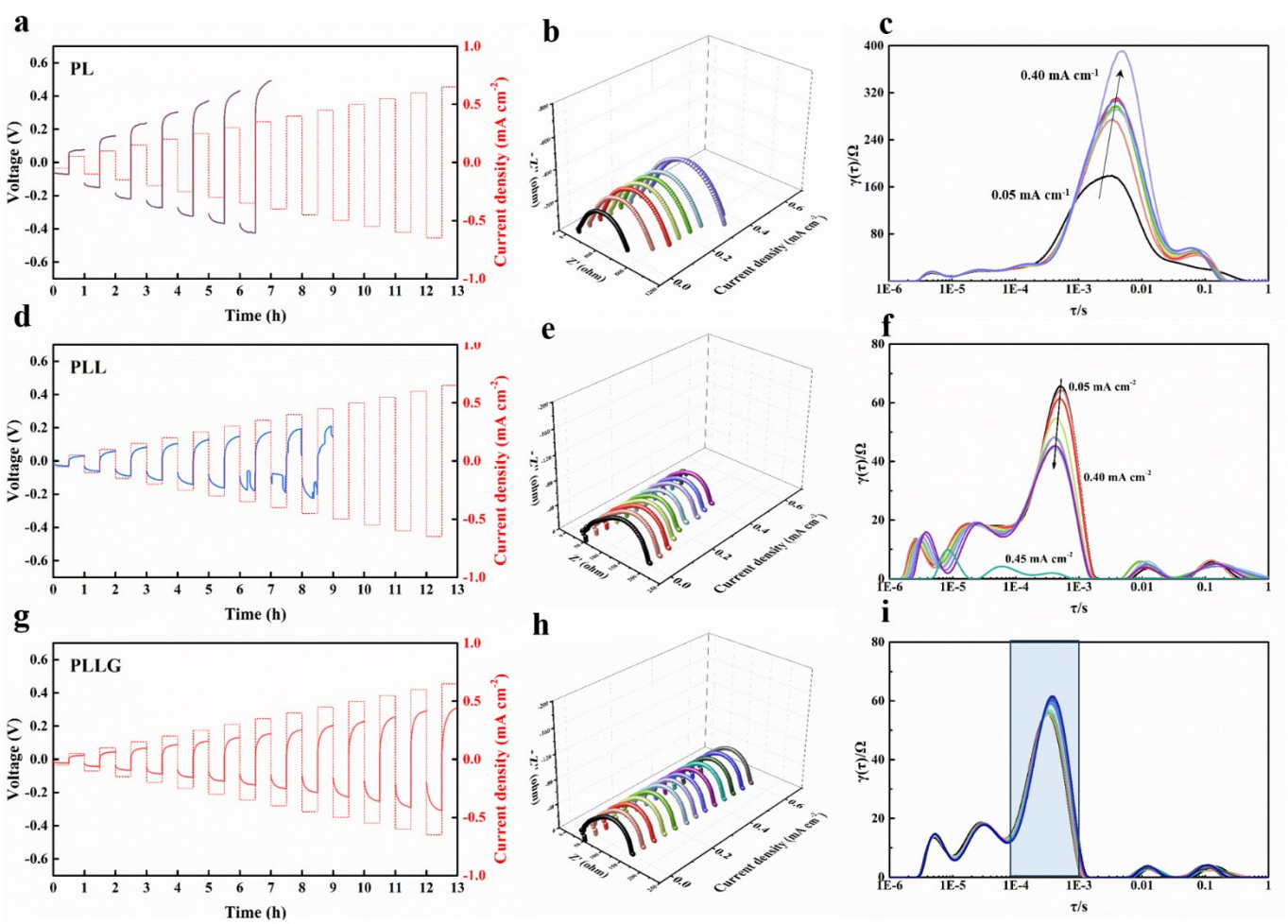

Fig. 5. Critical current density (CCD) tests of (a) Li/PL/Li cell, (d) Li/PLL/Li cell and (g) Li/PLLG/Li cell. EIS spectrums of (b) Li/PL/Li cell, (f) Li/PLL/Li cell and (h) Li/PLLG/Li cell during CCD test. DRT profiles of (c) Li/PL/Li cell, (f) Li/PLL/Li cell and (i) Li/PLLG/Li cell during CCD test.

Critical current density (CCD) of Li-Li symmetric cells based on each electrolyte was applied to further explore the effect of g-C_3N_4 additives on the interface stability against the Li metal anode. An increasing current density of 0.05 mA cm^{-2} per step from 0.05 to 0.65 mA cm^{-2} was employed to test the Li plating/stripping curves and subsequently recorded

by EIS spectra for each plating and stripping step, the voltage profiles reflect the electrolyte/Li interface behavior during cycling. The results of PL are shown in Fig. 5a, an overpotential as high as 0.5 V was observed at a current density of 0.35 mA cm^{-2} due to the sluggish movement of lithium ions through the PEO segments. Meanwhile, the middle-frequency region of the EIS spectra (corresponding to the interfacial impedance) increased after the first 0.05 mA cm^{-2} cycle (Fig. 5b), indicating an unstable electrolyte/Li interface. Although Li-Li symmetric cell based on PLL presents a lower initial overpotential than PL, a dropped voltage was observed at the 0.35 mA cm^{-2} step (Fig. 5d), reflecting an initial short circuit in the electrolyte. The subsequently recovered voltage profile may be linked to the fusing of lithium dendrites. This interfacial recovery did not lead to a significant change in the EIS spectra of the PLL when the current density $\leq$ 0.4 mA cm^{-2}, as shown in Fig. 5e. At the current density of 0.45 mA cm^{-2}, the suddenly dropped semicircle could be assigned to the growth of lithium dendrites that substantially reduced the impedance. In contrast to PLL, PLLG exhibits highly reversible Li plating and stripping at each increasing current density step. There is no instability observed in the voltage profile (Fig. 5g) and interfacial impedance fluctuation (Fig. 5h) in PLLG, indicating that the addition of g-C_3N_4 enables a stable electrolyte/Li interface with a high current density endurance.

The distribution of relaxation time (DRT) [68] was employed to analyze the Li transportation kinetics in SPEs during Li plating/stripping in the CCD tests. First, the EIS spectra of PLL-based Li-Li symmetric cells at different temperatures were measured to identify the isolated kinetic processes in the cells (Fig. S25a). The DRT spectra are summarized in Fig S25b. According to the DRT spectra at different temperatures, the kinetic process of the Li-Li symmetric cell at 60℃ could be divided into three parts: (1) The time constant in the range of 10^{-6} to 10^{-5} s can be attributed to electrode contact impedance between current collector, Li metal and electrolyte [69]; (2) the time constant in the range of 10^{-5} to 10^{-4} s is

related to the Li-ions conduction at the grain boundary of LATP particles and interfaces with polymer [70]; (3) the time constant in the range of 10^{-4} to 10^{-3} s could be assigned to the ionic diffusion through anode-electrolyte interface and solid electrolyte interphase (SEI) [71]. Compared with PL, both PLL and PLLG exhibit an order of magnitude faster Li-ion transport on the electrode-electrolyte interface (Figs. 5c, 5f and 5i). The downtrend in SEI resistance of PLL during cycling could be attributed to the thinning of the electrolyte film by the growth of Li dendrites [72], and a significant decrease in the interface/SEI resistance was observed after 0.45 mA cm^{-2} step (irreversible short circuit). In Fig. 5f, the shift in contact impedance between $\tau = 10^{-5}$ to 10^{-4} s also indicates degradation of electric contact and ion diffusion path in PLL. As shown in Fig. 5i, there was no significant change in contact impedance during cycling, indicating that the electrolyte/Li interface maintains a well-connection during Li plating/stripping. The enhanced interfacial stability in PLLG leads to an extremely stable SEI impedance during cycling [73]. Based on SEM, XPS and DRT characterizations, we suggest that the addition of g-C_3N_4 effectively stops the Li dendrite growth by optimizing the SEI composition and improving the anode-electrolyte interfacial compatibility.

Conclusion

In summary, we demonstrate that g-C_3N_4 filler can optimize the interfacial stability of Li metal anodes in PEO-based SPEs. g-C_3N_4 nanosheets act as an anion acceptors and nano-capacitances in SPEs, immobilizing the facile movement of the $TFSI^-$ group in the matrix and smoothed the electric field on the electrode-electrolyte interface, which effectively reduces the concentration polarization during cycling and enables a uniform Li^+ flux. The aforementioned strategy of anchoring anions increases the Li-ion transference number. DFM also revealed that at the electrolyte-anode interface, a higher dielectric region derived from the g-C_3N_4 additive can result in a dipole layer arranged near the anode surface that can guide the lithium ions into

a more uniform path. On the other hand, the nitrogen-containing groups in the g-C_3N_4 adsorbed at the interface of the lithium metal anode promote the uniform deposition of lithium at the interface as confirmed by DRT characterizations. The introduction of g-C_3N_4 effectively increased the ionic conductivity to 6.46×10^{-4} S cm^{-1}. Due to the stable interfacial layer, the Li-Li symmetric battery based on the PLLG composite electrolyte has low polarization voltage and enables Li-dendrites-free ASSLMBs in high current density. The $LiFePO_4$/PLLG/Li battery can deliver a stable charge/discharge capacity of 121.6 mAh/g at 1 C current density, as well as good rate performance.

Declaration of competing interest

The authors declare that they have no known competing financial interests or personal relationships that could have appeared to influence the work reported in this paper.

Acknowledgements

The authors acknowledge the financial support by the National Natural Science Foundation of China (No. 61574037, 11874113, 11344008, 11204038, 22179020), Foreign Science and technology cooperation project of Fuzhou Science and Technology Bureau (No. 2021-Y-086), Industry-university Cooperation Project of Fujian Province (No. 2020H06027), the Faraday Institution (grant number FIRG018), and EPSRC project EP/V00767X/1.

References

[1] Y. Q. Chen, Y.Q. Kang, Y. Zhao, et al., J. Energy Chem. 59 (2021) 83-99.

[2] A. Manthiram, X.W. Yu, S.F. Wang, Nat. Rev. Mater. 2 (2017) 16103.

[3] X.Q. Zhang, X.B. Cheng, Q. Zhang, Adv. Mater. Interfaces 5 (2018) 1701097.

[4] Q. Liu, Z. Geng, C.P. Han, et al., J. Power Sources 389 (2018) 120-134.

[5] J. Lu, Y. Li, J. Mater. Sci. Mater. Electron. 32 (2021) 9736–9754.

[6] S. Yubuchi, S. Teragawa, K. Aso, et al., J. Power Sources 293 (2015) 941-945.

[7] Y. Kato, S. Hori, R. Kanno, Adv. Energy Mater. 10 (2020) 2002153.

[8] Q. Zhao, S. Stalin, C.Z. Zhao, L. Archer, Nat. Rev. Mater. 5 (2020) 229-252.

[9] Y. Guo, S.C. Wu, Y.B. He, et al., eScience 2 (2022) 138-163.

[10] J.N. Feng, L. Wang, Y.J. Chen, et al., Nano Convergence 8 (2021) 2.

[11] Y.X. Wu, Y. Li, Y. Wang, et al., J. Energy Chem. 64 (2022) 62-84.

[12] F. Yuan, H.Z. Chen, H.Y. Yang, et al., Mater. Chem. Phys. 89 (2005) 390-394.

[13] S. Jian, Y. Cao, W. Feng, et al, Materials Today Sustainability 20 (2022) 100224

[14] Y. Zhao, L. Wang, Y.N. Zhou, et al., Adv. Sci. 8 (2021) 2003675.

[15] D.X. Cao, X. Sun, Q. Li, et al., Matter 3 (2020) 57-94.

[16] P.H. Yao, H.B. Yu, Z.Y. Ding, et al., Front. Chem. 7 (2019) 522.

[17] S.L. Liu, W.Y. Liu, D.L. Ba, et al., Adv. Mater. 35 (2023) 2110423.

[18] Y.W. Song, K. Heo, J. Lee, et al., RSC Adv. 11 (2021) 31855-31864.

[19] H. Zhuang, W.C. Ma, J.W. Xie, et al., J. Alloys Compd. 860 (2021) 157915.

[20] X. Guo, Z.Y. Ju, X.T. Qian, et al., Angew. Chem. Int. Ed. 62 (2023) 202217538.

[21] L. Su, A. Manthiram, Small Struct. 3 (2022) 2200114.

[22] J. Chazalviel, Phys. Rev. A 42 (1990) 7355-7267.

[23] B. Ghanbarzadeh, A. Khatibi, A. Asadi, B. Shokri, J. Energy Storage 47 (2022) 103668.

[24] Z.L. Li, S.X. Wang, J.K. Shi, et al., Energy Stor. Mater. 47 (2022) 262-270.

[25] Z.J. Ju, Q.F. Xie, O.W. Sheng, et al., Nano Lett. 22 (2022) 5473-5480.

[26] C. Li, Z.Y. Liang, Z.Z. Li, et al., Nano Lett. 23 (2023) 4014-4022.

[27] R. Xu, X.B. Cheng, C. Yan, et al., Matter 1 (2019) 317-344.

[28] Z.X. Wang, Z.P. Cai, M.N. Liu, et al., ACS Omega 8 (2023) 16411-16418.

[29] K.R. Deng, T.Y. Guan, F.H. Liang, et al., J. Mater. Chem. A 9 (2021) 7692-7702.

[30] S. Anna, M. Maciej, S. Jarosław, et al., Appl. Phys. A 129 (2023) 37.

[31] H.Y. Yuan, J.Y. Luan, Z.L. Yang, et al., ACS Appl. Mater. Interfaces 12 (2020) 7249–7256.

[32] X.X. Wu, K.Y. Chen, Z.G. Yao, et al., J. Power Sources 501 (2021) 229946.

[33] O. Chae, B. Lucht, Adv. Energy Mater. 13 (2023) 2203791.

[34] D.C. Zhang, Z.B. Liu, Y.W. Wu, et al., Adv. Sci. 9 (2022) 2104277.

[35] C.C. Chang, Y. Yao, R.R. Li, et al., Nano Energy 93 (2022) 106871.

[36] M. Majdoub, Z. Anfar, A. Amedlous, ACS Nano 14 (2020) 12390-12469.

[37] Z.J. Sun, Y.H. Li, S.Y. Zhang, et al., J. Mater. Chem. A 7 (2019) 11069-11076.

[38] J.L. Hu, K.Y. Chen, Z.G. Yao, C.L. Li, Sci. Bull. 66 (2021) 694-707.

[39] Y. Huang, B. Chen, J. Duan, et al., Angew. Chem. Int. Ed. 59 (2020) 3699-3704.

[40] J.L. Liu, Y.Q. Zhang, L. Zhang, et al., Adv. Mater. 31 (2019) 1901261.

[41] Y. Xu, T. Li, L.P. Wang, Y.J. Kang, Adv. Mater. 31 (2019) 1901662.

[42] P.B. Zhai, T.S. Wang, H.N. Jiang, et al., Adv. Mater. 33 (2021) 2006247.

[43] Y.T. He, Y.H. Zhang, H.M. Sari, Nano Energy 89 (2021) 106334.

[44] O. Castañeda-Uribe, R. Reifenberger, A. Raman, et al., ACS Nano 9 (2015) 2938-2947.

[45] J. Hadi, S. Aziz, M. Mustafa, et al., J. Mater. Res. 9 (2020) 9283-9294.

[46] J. Dygas, Solid State Ionics 176 (2005) 2065-2078.

[47] V. St-Onge, M. Cui, S. Rochon, et al., Commun. Mater. 2 (2021) 83.

[48] Y. Huang, Z. Zhang, H. Gao, J. Huang, C. Li, Solid State Ionics 356 (2020) 115437.

[49] W.Y. Li, Y. Pang, J.Y. Liu, et al., RSC Adv. 7 (2017) 23494-23501.

[50] L. Aguilera, S. Xiong, J. Scheers, A. Matic, J. Mol. Liq. 210 (2015) 238-242.

[51] X.Y. Yang, J.X. Liu, N.B. Pei, et al., Nano-Micro Lett. 15 (2023) 74.

[52] Y. Lin, J.B. Wu, X.H. Huang, et al., Ionics 25 (2019) 5697-5707.

[53] J.J. Wu, X.Q. Ji, X.H. Yuan, et al., Chem. Mater. 31 (2019) 9188−9199.

[54] X.Y. Chen, D.H. Kou, D.F. Lu, RSC Adv. 6 (2016) 66814-66821.

[55] H.X. Xu, T.T. Zhang, Y. Gu, et al., Mikrochim Acta 187 (2020) 163.

[56] I. Elashmawi, L. Gaabour, Results Phys. 5 (2015) 105-110.

[57] N. Zhang, J.W. He, W.M. Han, et al., J. Mater. Sci. 54 (2019) 9603-9612.

[58] A. Karmakar, A. Ghosh, Curr. Appl. Phys. 12 (2012) 539-543.

[59] Q. Kang, Z.C. Zhuang, Y. Li, et al., Nano Res. (2023) 1-10.

[60] X. Lou, J. Zhong, D. Cheng, et al., Chem. Eng. J. 468 (2023), 143681.

[61] J.M. Tao, D.Y. Wang, Y.M. Yang, et al., Adv. Sci. 9 (2021) 2103786.

[62] X. Liu, W.N. Mao, J. Gong, et al., Polymers 15 (2023) 394.

[63] X. Ao, X.T. Wang, J.W. Tan, et al., Nano Energy 79 (2021) 105475.

[64] X.Q. Zhang, X. Chen, L.P. Hou, et al., ACS Energy Lett. 4 (2019) 411-416.

[65] M. Lacey, A. Yalamanchili, J. Maibach, et al., RSC Adv. 6 (2016) 3632-3641.

[66] S.F. Liu, X.H. Xia, S.J. Deng, et al., Adv. Mater. 31 (2019) 1806470.

[67] X.Y. Chang, H.Q. Fan, L. Lei, et al., Catalysts 13 (2023) 269.

[68] T. Paul, P. Chi, P. Wu, M. K. Wu, Sci. Rep. 11 (2021) 12624.

[69] Y. Lu, C.Z. Zhao, R. Zhang, et al., Sci. Adv. 7 (2021) eabi5520.

[70] P. Vadhva, J. Hu, M. Johnson, et al., Chem. Electro. Chem. 8 (2021) 1930-1947.

[71] C.C. Sheng, F.J. Yu, C.M. Li, et al., J. Phys. Chem. Lett. 12 (2021) 2064-2071.

[72] Z.W. Wang, L. Zhang, X. Shang, et al., Chem. Eng. J. 428 (2022) 132094.

[73] R.F. Song, J.M. Yao, R.N. Xu, et al., Adv. Energy Mater. 13 (2023) 2203631